

Single-Shot Optical Neural Network

LIANE BERNSTEIN^{1,3}, ALEXANDER SLUDDS¹, CHRISTOPHER PANUSKI¹, SIVAN TRAJTENBERG-MILLS¹, RYAN HAMERLY^{1,2}, AND DIRK ENGLUND¹

¹*Research Laboratory of Electronics, Massachusetts Institute of Technology, 50 Vassar St, Cambridge, MA 02139, USA*

²*NTT Research, Inc., Physics & Informatics Laboratories, Sunnyvale, CA 94085, USA*

³*lbern@mit.edu*

Abstract:

As deep neural networks (DNNs) grow to solve increasingly complex problems, they are becoming limited by the latency and power consumption of existing digital processors. ‘Weight-stationary’ analog optical and electronic hardware has been proposed to reduce the compute resources required by DNNs by eliminating expensive weight updates; however, with scalability limited to an input vector length K of hundreds of elements. Here, we present a scalable, single-shot-per-layer weight-stationary optical processor that leverages the advantages of free-space optics for passive optical copying and large-scale distribution of an input vector and integrated optoelectronics for static, reconfigurable weighting and the nonlinearity. We propose an optimized near-term CMOS-compatible system with $K = 1,000$ and beyond, and we calculate its theoretical total latency (~ 10 ns), energy consumption (~ 10 fJ/MAC) and throughput (\sim petaMAC/s) per layer. We also experimentally test DNN classification accuracy with single-shot analog optical encoding, copying and weighting of the MNIST handwritten digit dataset in a proof-of-concept system, achieving 94.7% (similar to the ground truth accuracy of 96.3%) without retraining on the hardware or data preprocessing. Lastly, we determine the upper bound on throughput of our system (~ 0.9 exaMAC/s), set by the maximum optical bandwidth before significant loss of accuracy. This joint use of wide spectral and spatial bandwidths enables highly efficient computing for next-generation DNNs.

1. Introduction

Artificial deep neural networks (DNNs) have revolutionized automation in many tasks such as image classification [1], natural language processing [2] and medical prediction and diagnosis [3]. These breakthroughs were made possible by sufficiently large datasets, computing capacity and DNN models [4]. Though specialized hardware has accelerated DNN processing significantly in data centers [5–7], modern DNNs have continued to grow exponentially in numbers of parameters and operations, and processors are not keeping pace [4]. Inference, which accounts for 80-90% of machine learning workloads in data centers [8], has particularly stringent requirements for low latency, such as in translation and autonomous driving, as well as in more recent applications in astrophysics [9], particle physics [10], and the control of fusion reactors [11].

The rate-limiting step in DNN inference is matrix multiplication, e.g., where a matrix of learned weights multiplies an input vector. More specifically, the most expensive task within matrix-vector multiplication (MVM) is data movement of the weights and inputs from memory to the multiplier units, followed by the multiply-accumulate (MAC) operation itself [7, 12]. Static, passive ‘weight-stationary’ architectures [12, 13] (e.g., in-memory computing [14, 15]) can yield significant improvements in efficiency: in this dataflow, the input vector is broadcast across the multiplier units that apply fixed weights, and the output vector can, in theory, be read out in one step. DNN layer outputs can thus be computed in a single shot without costly weight updates — if the entire weight matrix can be stored on the hardware.

DNN hardware accelerators have previously been configured in a weight-stationary dataflow [7,

16–21]. However, this work does not simultaneously satisfy low latency and energy consumption along with scalability. In digital electronic circuits (e.g., Google’s TPU [7]), constraints on wiring for digital data transmission require partial products to be passed from one multiplier to the next at each clock cycle, which prohibits single-shot readout. Analog electronic circuits such as memristor crossbar arrays [16, 17], on the other hand, can sum partial products along a wire by Kirchhoff’s current law, but they are bounded in speed, energy consumption and accuracy by parasitic capacitance, resistance and current leakage [22, 23]. Integrated 2D optical schemes can compute at very high speeds [19–21], but an input vector of length K must travel through elements of $\mathcal{O}(K)$ depth, and scalability is bounded by error accumulation and constraints on control, multiplexing, component area and insertion and waveguide loss.

A 3D optical architecture, on the other hand, permits higher connectivity between potentially millions of spatial modes. 3D optical MVM accelerators were among the first to be investigated by pioneers in the field [24–27] — partly out of necessity (prior to the advent of compact low-loss photonic integrated circuits) — but they did not achieve widespread adoption. Firstly, competition from digital electronic computers limited their application space [28, 29]. Secondly, they suffered from a lack of flexibility, where experimental demonstrations employed fixed weighting masks or bulky modulators and were small in scale (input vectors with ~ 10 s of elements). Recently, a resurgent interest in 3D optical processors has been driven by theoretical analyses showing the potential of ultra-low energy computing for DNNs [30, 31], which was experimentally validated for vector-vector dot products [32] or short input vectors (56 elements) [33]. Other custom configurations required retraining [34–36].

Here, we present a scalable, single-shot-per-layer 3D optical neural network, where integrated sources encode an input vector and free-space optical elements distribute and copy this display (*fan-out*) to passive optoelectronic weighting elements. Kirchhoff’s current law sums the partial products in analog electronics and a simple comparator implements the nonlinearity. This architecture combines the advantages of both free-space optics (tightly packed spatial modes) and integrated optoelectronics (passive weighting and a low-power nonlinearity) to enable scalability. We first describe an optimized near-term, CMOS-compatible implementation and calculate the theoretical latency (~ 10 ns), energy consumption (~ 10 fJ/MAC) and throughput (\sim petaMAC/s) to process a complete million-element DNN layer. Next, we experimentally demonstrate low loss of classification accuracy of the MNIST handwritten digit dataset with proof-of-concept analog optical encoding of the input vector, free-space optical fan-out and analog optical weighting. Dynamic reconfigurability of the inputs, fan-out and weighting elements allow for potential model updates. We then calculate the physical limit to throughput of our system (~ 0.9 exaMAC/s) by measuring classification accuracy versus source spectral width. These energy and latency specifications can enable next-generation DNNs while also having a significant impact on other fields such as Ising machines, complex optimization, and other machine-learning tasks where MVM also dominates energy consumption and latency.

2. Architecture

Figure 1 illustrates single-shot computation of a DNN layer in inference. In a fully connected neural network (Fig. 1(a-b)), a layer’s output (\mathbf{y}) is the weighted sum of the inputs (\mathbf{x}), where the weights (\mathbf{W}) have been pre-learned during the training phase. In other words, a fully connected layer is equivalent to MVM, with $\mathbf{y}_{N \times 1} = f(\mathbf{W}_{N \times K} \cdot \mathbf{x}_{K \times 1})$, where a nonlinear function (f) approximates the thresholding operation in the brain [12]. Convolutional layers can also be implemented by matrix multiplication, e.g., using a Toeplitz matrix. In Fig. 1(c), \mathbf{x} is recast into blocks and projected onto each row of \mathbf{W} . (In many tasks, such as image classification, the input \mathbf{x} is already a 2D image that can be processed directly.) With the inputs then local to their corresponding weights, all required element-wise multiplications are performed simultaneously. Free-space optics can passively implement this data routing, replication and

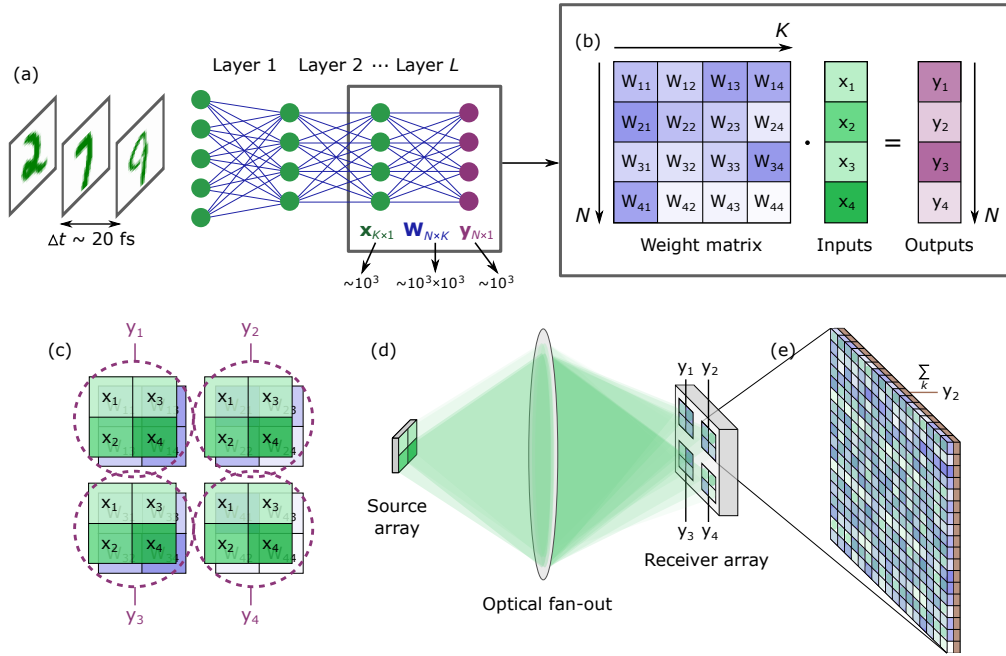


Fig. 1. A fully connected neural network yields outputs \mathbf{y} after L layers of computation (a). In one layer (b), weight matrix $\mathbf{W}_{N \times K}$ multiplies input activation vector $\mathbf{x}_{K \times 1}$ followed by a nonlinearity (e.g., Rectified Linear Unit, not shown) to produce output activation vector $\mathbf{y}_{N \times 1}$. This matrix-vector product can be computed in one time step (c) with block encoding and fan-out of \mathbf{x} over the rows of \mathbf{W} and block-wise summation. In (d), a K -element source array encodes \mathbf{x} into the analog intensities of light pulses, which are replicated and imaged onto N receiver blocks, each with K static weighting devices. Electronics perform the summation of element-wise products and the nonlinearity. Outputs are broadcast to the next layer, which can be implemented with a duplicate of the same hardware. An expanded view of one block in (e) shows that free-space optics enable high-density, 3D information transfer, with $\sim 10^3$ inputs incident on $\sim 10^3$ weighting elements per block above electrically connected photodetectors.

weighting (Fig. 1(d-e)).

In our scheme, a 4f system performs this single-shot MVM (Fig. 2). A source array encodes the input activations \mathbf{x} into the single-spatial-mode analog amplitudes of light pulses in the object plane. These sources can operate at \sim GHz rates, e.g., with vertical-cavity surface-emitting lasers (VCSELs) or μ LEDs [37–39]. In the Fourier plane, a diffractive optical element (DOE) displays a spot array generation pattern. The DOE can be implemented with array of optical phase change material (O-PCM) cells [40–42] or a fixed phase mask for passive fan-out. The spot array in the image plane generated by the DOE is optically convolved with the image of the input pattern, which yields N copies of the input pattern. Reconfigurable optoelectronic weighting elements then attenuate the intensity of each replicated input pixel proportionally to each weight value in \mathbf{W} . The weighting elements can also be an array of O-PCM pixels or other elements without passive energy consumption, such as MEMS modulators [43], placed directly above fast, μ m-scale photodetectors (PDs) [44, 45]. Kirchhoff’s current law then performs the block-wise summation electronically. Equivalently, the PD block can be replaced by a single large PD per block for ‘optical fan-in’ — this solution is similar to individual μ m-scale PDs since different diffraction-limited spatial modes at the same wavelength and polarization cannot overlap by the

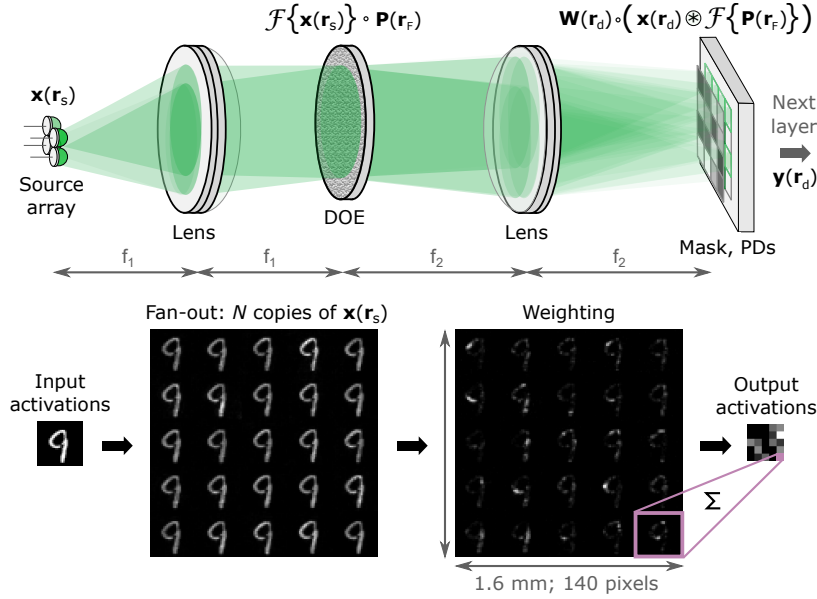


Fig. 2. Single-shot optical neural network. A source array of wavelength λ in the object plane encodes the inputs $\mathbf{x}(\mathbf{r}_s)$ into analog optical intensities, where \mathbf{r}_s is the spatial position in the 2D source plane perpendicular to the optical axis. To generate N copies of $\mathbf{x}(\mathbf{r}_s)$, a diffractive optical element (DOE) in the Fourier plane performs element-wise multiplication of the spatial Fourier transform of $\mathbf{x}(\mathbf{r}_s)$ with a fan-out phase pattern $\mathbf{P}(\mathbf{r}_F)$, where $\mathbf{r}_F = 2\pi \cdot \mathbf{r}_s / (\lambda \cdot f_1)$. Optoelectronic weighting elements in a reconfigurable mask in the image plane perform element-wise products between the weight matrix and the replicated input activations: $\mathbf{W}(\mathbf{r}_d) \circ (\mathbf{x}(\mathbf{r}_d) \otimes \mathcal{F}\{\mathbf{P}(\mathbf{r}_F)\})$, where $\mathbf{r}_d = -(f_1/f_2) \mathbf{r}_s$. Photodetectors (PDs) convert the signal to the electrical domain, and Kirchhoff's current law sums the K elements in each of the N blocks. After the electronic nonlinearity, the outputs can be optically broadcast to the next layer. Experimental fan-out and weighting data shown, with $K \times N = (28 \times 28) \times (5 \times 5) = 140 \times 140 = 19,600$ pixels.

Second Law of Thermodynamics [46]. A transimpedance amplifier (TIA) per block reads out the accumulated charge and an electronic post-processing unit performs the nonlinearity to yield \mathbf{y} . An output source array with one source per block is then the input to the next layer.

We describe the latency, throughput and energy calculations for an optimized, CMOS-compatible system with $N = K = 1,000$ in Supplement 1, Section 1. In brief, the latency of ~ 10 ns is the summed update time of the electronic elements and the optical time of flight. Because operations are pipelined to compute 10^6 MACs every ~ 1 ns, the system computes $\sim 10^{15}$ MAC/s — a throughput on the order of petaMAC/s. The energy is ~ 10 fJ/MAC, including a source wall-plug efficiency of 10% [37–39], PD responsivity of 0.2 A/W [44,45], TIA sensitivity of 1 μ A at 1 GHz [47] and TIA, ADC, DAC and nonlinearity energies of 1 pJ per operation [7, 12, 47–50]. We compare these figures to the state of the art in the Discussion section below.

3. Experimental demonstration

3.1. Experimental setup

We experimentally verified the impact of analog optical data encoding, fan-out and weighting on the classification accuracy of a two-hidden-layer fully connected DNN with $784 \rightarrow 25 \rightarrow 25 \rightarrow 10$ activations. Figure 3(a) shows our setup, with additional details provided in Supplement 1, Section 2. A liquid crystal on silicon spatial light modulator (LCoS SLM) displays an input image

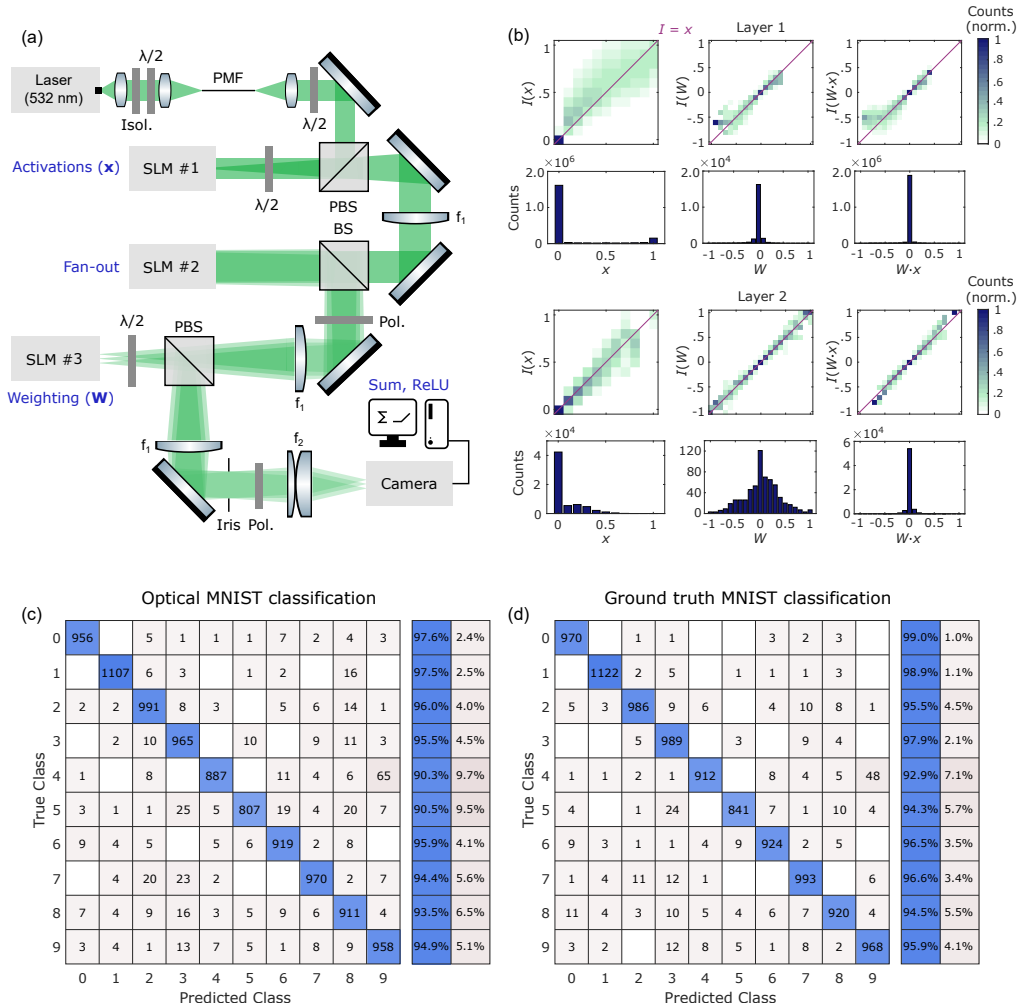


Fig. 3. Proof-of-concept implementation of single-shot optical neural network. (a) Laser light centered at 532 nm travels through an isolator (Isol.) into a single-mode polarization-maintaining fiber (PMF). Half-wave plates ($\lambda/2$) rotate the collimated beam's polarization to 45° on a spatial light modulator (SLM #1) in the object plane, which encodes the input activations (x) by pixel-wise polarization rotation. The polarizing beamsplitter (PBS) then translates the polarization encoding to intensity modulation. In the Fourier plane, SLM #2 imparts a fan-out phase pattern. Two-inch achromatic lenses of equal focal lengths $f_1 = 250$ mm image the replicated input activations from SLM #1 to SLM #3 for pixel-wise weighting (W). An achromatic lens of focal length $f_1 = 250$ mm and an achromatic lens pair with $f_2 = 145$ mm (individual focal lengths of 750 mm and 180 mm) map SLM #3 pixels to the camera. A digital computer controls the hardware, sums each block and implements the nonlinearity. (b) Histograms show received intensities I (normalized) versus transmitted values over all pixels for activations x , weights W and element-wise products $W \cdot x$ from 100 randomly selected test images for the first and second layers of the DNN. Each column is normalized by the sum of the column ('Counts' in 1D histograms below each 2D histogram for reference). Purple lines illustrate ideal performance along the diagonal. (c) Confusion matrix for classification of 10,000 previously unseen MNIST test images by our optical system (94.7% accuracy), and in (d), by a standard digital computer (96.3% accuracy).

\mathbf{x} by pixel-wise amplitude modulation of a collimated 532 nm continuous-wave (CW) laser diode. In the Fourier plane, a second LCoS SLM imparts a phase pattern for fan-out. In the image plane, a third LCoS SLM displays a complete weight matrix for pixel-wise attenuation (multiplication) of the replicated inputs. A telescope relays the image of the third SLM to a camera connected to a digital electronic computer that controls the hardware, sums each block of weighted inputs and performs the nonlinearity (Rectified Linear Unit, ReLU). The electronic computer also multiplies pixel values that should be negatively weighted by -1 , since the SLM can only apply the absolute values of the weights. In practice, this negative weighting can be implemented with an analog switch or two PDs per receiver pixel (see Supplement 1, Section 3). The layer outputs, which are always positive because of the ReLU nonlinearity, are then fed back to the first SLM, and the weights are updated for the next layer of computation. See Supplement 1, Section 4 for our image processing and one-time system calibration procedures.

Figure 3(b) illustrates the distributions of measured intensities I versus transmitted inputs x , weights W and element-wise dot products $W \cdot x$, normalized by the sum of each column. To determine $I(x)$, we displayed MNIST test images on SLM #1 and set all SLM #3 pixels to a constant, uniform value. Similarly, to measure $I(W)$, we displayed the layer weights on SLM #3 and set SLM #1 pixels to a constant, uniform value. The distribution $I(W \cdot x)$ versus $W \cdot x$ for layer 1 is broad for $W \cdot x \in [-1, -0.5]$, but these columns only represent 0.06% of the total counts. Otherwise, $I(W \cdot x)$ is close to the diagonal $I = W \cdot x$. The distributions of I for layer 2 are narrower than those for layer 1 due to increased pixel spacing made possible by fewer input activations (see Supplement 1, Section 2), which lowers crosstalk.

3.2. MNIST classification

We performed inference on the MNIST handwritten digit dataset with the two-hidden-layer DNN described above — see Supplement 1, Section 5 for the training procedure on a standard digital electronic computer. Using our optical setup, we obtained a 94.7% classification accuracy of the full MNIST test set of 10,000 previously unseen images, compared with the ground-truth all-electronic accuracy of 96.3%. See Fig. 3(c-d) for corresponding confusion matrices. Our optical hardware’s classification error was $\sim 1\%$ higher than the ground truth for most digits, but up to $\sim 4\%$ higher for the digit ‘5’ (additionally misclassified ‘5’s were mostly labeled ‘6’ or ‘8’ by our ONN, possibly due to blurring from crosstalk). The top-2 optical accuracy was 98.1%, similar to the ground truth top-2 accuracy of 98.7%.

3.3. Optical throughput

Next, we investigated the optical limit to throughput of our system. In other words, we determined the upper bound on the number of information-carrying pulses that can be transmitted per second before significant loss of classification accuracy. To do so, we measured the source spectral width at which the classification error doubles, where a source’s minimum pulse duration is inversely related to its spectral width by the time-frequency Fourier transform relationship. We thus repeated the inference experiment described in the section above, but replaced the CW laser with a tunable supercontinuum source. As Fig. 4 shows, a broader source spectrum decreases classification accuracy because it yields blurred outputs: by the spatial Fourier transform relationship between the Fourier and image planes, the distance between each replicated input pattern and the optical axis is linear in wavelength (see theory in Supplement 1, Section 6). The experimental classification error of 1,000 images from the MNIST test set doubled from 5.4% with the CW diode to 10.8% at a spectral width of 21 nm, where we define spectral width as twice the RMS width of the spectrum ($2\sigma_\lambda$, i.e., twice the standard deviation) to account for its irregular shape. The Fourier transform of the corresponding source spectrum (resampled from linear in wavelength to linear in frequency $\nu = c/\lambda$) yields a pulse of full width at half maximum ~ 0.02 ps. Therefore, given a transform-limited source in an optimized implementation,

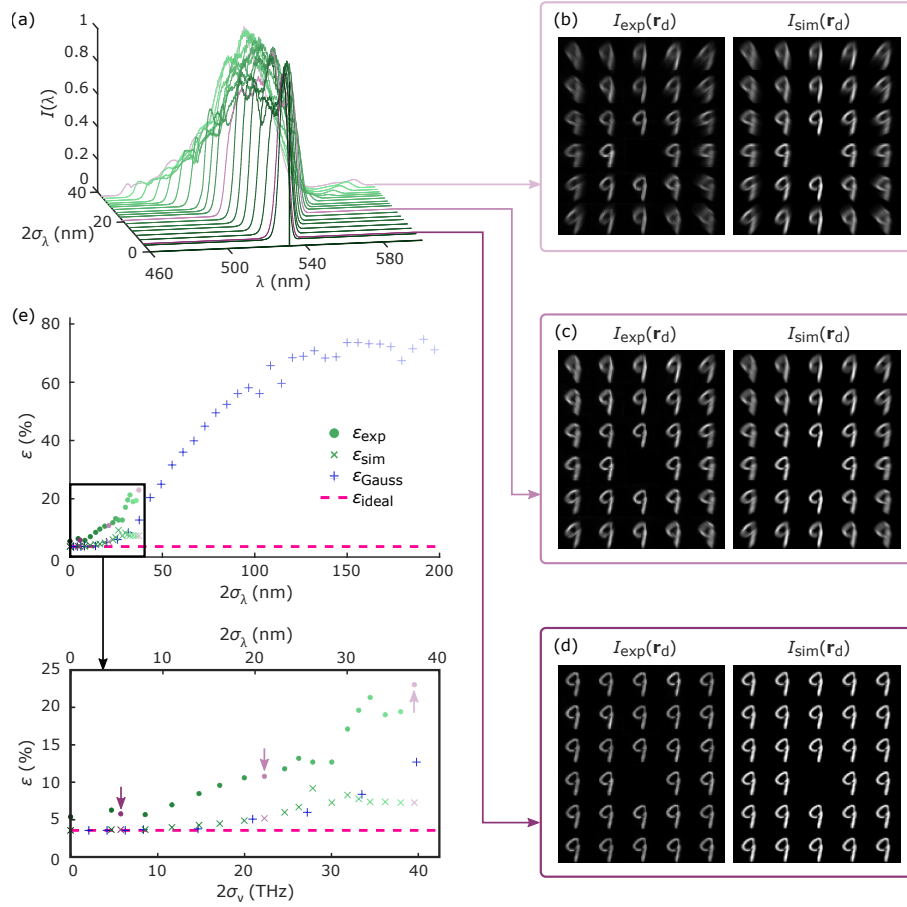


Fig. 4. A supercontinuum laser with filtered spectra (a) replaces the continuous-wave diode in our single-shot ONN demonstration and causes blurring. Example blurred images in (b-d) with spectral widths of 37 nm, 21 nm and 5.4 nm and measured classification errors of 23%, 11% and 5.8%, respectively. Element [4,3] is skipped because it overlaps with the zero order from SLM #2 — we replace it with element [6,4] in our DNN experiments. Left images measured on the camera and right images show simulated blurring from measured spectra (see Supplement 1, Section 6). (e) Classification error of two-hidden-layer fully connected neural network with 25 activations per hidden layer on 1,000 previously unseen MNIST test images versus spectral width ($2 \times$ RMS width, i.e., $2\sigma_\lambda$). Measured error from experiment (ϵ_{exp}) is higher than the simulated error calculated from the source spectra (ϵ_{sim}), but follows a similar trend to the simulated error calculated from Gaussian spectra with broader bandwidths (ϵ_{Gauss}). ϵ_{ideal} shows ground truth error without blurring.

the maximum throughput in the first layer is the number of multiply-accumulate operations (# MACs = $28 \times 28 \times 25$) divided by the minimum pulse length, which yields ~ 0.9 exaMAC/s. Emerging high-speed modulators, e.g., plasmonic electro-optic modulators [51, 52] or thin-film lithium niobate [53], could potentially allow us to achieve this near-exascale throughput.

4. Discussion

We have introduced a scalable optical neural network that can compute DNN layer outputs in a single shot. We first described a near-term optimized implementation and calculated that with existing CMOS-compatible technologies, it could compute a million-element MVM in ~ 10 ns, with an energy consumption of ~ 10 fJ/MAC and a throughput of \sim petaMAC/s. In such a weight stationary system, latency is independent of vector length as long as the weight matrix fits onto the hardware — we discuss limits to scalability below. In systolic arrays like Google’s TPU [7], on the other hand, since inputs are message-passed across the weight matrix, the latency is at least $N + K$ clock cycles for an $(N \times K)$ -sized MVM. The latency scaling is similar in output-stationary architectures [30, 31] since the inputs are streamed in over time. If $K = N = 1,000$, our optical processor then outperforms these architectures by two orders of magnitude. In energy consumption, digital DNN accelerators are limited primarily by data movement to ~ 0.1 - 1 pJ/MAC [7, 54, 55], depending on the implementation, process technology and workload. These values include peripheral logic and memory access, as well as the cost of one MAC operation (~ 25 fJ [56, 57]). The energy per MAC of our single-shot ONN, including E-O-E conversion, can thus be lower than the cost of a digital electronic MAC, without even factoring in expensive electronic data movement. An increase in source and detector efficiencies [46] could further reduce the energy consumption by an order of magnitude to the single-femtojoule per MAC regime. DAC and ADC costs may also be eliminated with analog electronic nonlinearities [22, 58], as analog output activations from one layer can be directly used as inputs to the next layer. The inputs to the first layer may also be in the analog domain, e.g., as they are read out from a sensor.

We demonstrated low loss of classification accuracy on the MNIST handwritten digit dataset with analog optical data encoding, fan-out and weighting (94.7% optical versus 96.3% ground truth). To increase classification accuracy further, we can reduce stray light on the detector. For example, higher fill-factor SLMs can lessen reflection from their backplanes, aberration-corrected lenses can focus spots more tightly in the image planes to lower crosstalk, and better optical coatings can decrease unwanted interference fringes. We can also run wider and deeper DNNs on the hardware (i.e., more neurons per hidden layer, a greater number of hidden layers and added biases). In future work, we will benchmark our system against other accelerators with standard DNNs such as LeNet [59] and AlexNet [1].

We then replaced the CW laser in our experiment with a filtered supercontinuum source to calculate the physical limit to throughput of our system. We measured the degradation of classification accuracy of the MNIST dataset as a function of optical source bandwidth, where a broader spectrum yielded blurred replicated input activations in the image plane. We found that a minimum pulse duration of 0.02 ps maintains the classification error within a factor of two. With $28 \times 28 \times 25$ multiplications per time step, this pulse width yields a near-exascale throughput limit. We obtained all above results without retraining on the hardware, which is preferred since retraining every processor on a large scale, e.g., in data centers, would be resource-intensive. However, to preserve accuracy for broader source spectra, we could modify our DNN to account for this expected blurring, e.g., by using the simulated blurred images as inputs to the DNN in training.

Our system is highly scalable thanks to tightly packed 3D free-space optical spatial modes (can be diffraction-limited to μm -scale) and passive, integrated optoelectronics (PDs and weighting elements such as O-PCM or MEMS). Because its components are CMOS compatible, it can be mass-produced, e.g., megapixel cameras with μm -scale PDs are readily available. Scalability is key in reducing the latency and energy consumption of DNNs: if the input data length K or DNN layer size $N \times K$ are larger than the hardware supports (i.e., if K is larger than ~ 100 elements in analog electronics or integrated optics), data need to be stored and fetched in memory over multiple time steps, in a process called ‘tiling’. Because memory access and data movement

are the current bottlenecks in state-of-the-art digital electronic DNN accelerators, hardware that does not address this memory access issue may not provide performance improvements over digital electronics for large problem sizes. In our system, increasing the matrix size further could reduce the energy consumption for a large workload as the fixed component costs would be amortized over a greater number of operations. However, since our scheme has no static power consumption, it is not critical to aim for 100% utilization.

In summary, we have presented a single-shot-per-layer optoelectronic inference machine and demonstrated low loss of classification accuracy with analog, reconfigurable optical processing. This scalable hardware with low resource consumption and the potential for ultra-high-speed computation can enable larger DNN models to carry out more complex tasks for next-generation artificial intelligence.

5. Backmatter

Funding. Natural Sciences and Engineering Research Council of Canada (PGSD3-517053-2018), NTT, National Science Foundation EAGER (CNS-1946976), National Science Foundation GRFP (1745302), and the U.S. Army Research Office through the Institute for Soldier Nanotechnologies (ISN) at MIT (W911NF-18-2-0048).

Acknowledgments. We thank Prof. David A. B. Miller for helpful discussions, Ian Christen for support with spectral measurements and the MITRE Corporation for the loan of one LCoS SLM.

Disclosures. The authors declare no conflicts of interest.

Data availability. Data underlying the results presented in this paper are available upon reasonable request.

Supplemental document. See Supplement 1 for supporting content.

References

1. A. Krizhevsky, I. Sutskever, and G. E. Hinton, "ImageNet classification with deep convolutional neural networks," in *Advances in Neural Information Processing Systems* 25, (2012), pp. 1097–1105.
2. T. Wolf, L. Debut, V. Sanh, J. Chaumond, C. Delangue, A. Moi, P. Cistac, T. Rault, R. Louf, M. Funtowicz, J. Davison, S. Shleifer, P. von Platen, C. Ma, Y. Jernite, J. Plu, C. Xu, T. Le Scao, S. Gugger, M. Drame, Q. Lhoest, and A. Rush, "Transformers: State-of-the-art natural language processing," in *Proceedings of the 2020 Conference on Empirical Methods in Natural Language Processing: System Demonstrations*, (Association for Computational Linguistics, 2020), pp. 38–45.
3. A. Esteva, A. Robicquet, B. Ramsundar, V. Kuleshov, M. DePristo, K. Chou, C. Cui, G. Corrado, S. Thrun, and J. Dean, "A guide to deep learning in healthcare," *Nat. medicine* **25**, 24–29 (2019).
4. X. Xu, Y. Ding, S. X. Hu, M. Niemier, J. Cong, Y. Hu, and Y. Shi, "Scaling for edge inference of deep neural networks," *Nat. Electron.* **1**, 216–222 (2018).
5. S. Bianco, R. Cadene, L. Celona, and P. Napoletano, "Benchmark analysis of representative deep neural network architectures," *IEEE Access* **6**, 64270–64277 (2018).
6. E. Nurvitadhi, G. Venkatesh, J. Sim, D. Marr, R. Huang, J. Ong Gee Hock, Y. T. Liew, K. Srivatsan, D. Moss, S. Subhaschandra *et al.*, "Can FPGAs beat GPUs in accelerating next-generation deep neural networks?" in *Proceedings of the 2017 ACM/SIGDA International Symposium on Field-Programmable Gate Arrays*, (Association for Computing Machinery, 2017), pp. 5–14.
7. N. P. Jouppi, C. Young, N. Patil, D. Patterson, G. Agrawal, R. Bajwa, S. Bates, S. Bhatia, N. Boden, A. Borchers *et al.*, "In-datacenter performance analysis of a tensor processing unit," in *Proceedings of the 44th Annual International Symposium on Computer Architecture*, (2017), pp. 1–12.
8. D. Patterson, J. Gonzalez, Q. Le, C. Liang, L.-M. Munguia, D. Rothchild, D. So, M. Texier, and J. Dean, "Carbon emissions and large neural network training," arXiv preprint arXiv:2104.10350 (2021).
9. C. E. Petrillo, C. Tortora, G. Vernardos, L. V. E. Koopmans, G. Verdoes Kleijn, M. Bilicki, N. R. Napolitano, S. Chatterjee, G. Covone, A. Dvornik, T. Erben, F. Getman, B. Giblin, C. Heymans, J. T. A. de Jong, K. Kuijken, P. Schneider, H. Shan, C. Spiniello, and A. H. Wright, "LinKS: discovering galaxy-scale strong lenses in the Kilo-Degree Survey using convolutional neural networks," *Mon. Notices Royal Astron. Soc.* **484**, 3879–3896 (2019).
10. J. Duarte, S. Han, P. Harris, S. Jindariani, E. Kreinar, B. Kreis, J. Ngadiuba, M. Pierini, R. Rivera, N. Tran, and Z. Wu, "Fast inference of deep neural networks in FPGAs for particle physics," *J. Instrumentation* **13**, P07027–P07027 (2018).

11. J. Degraeve, F. Felici, J. Buchli, M. Neunert, B. Tracey, F. Carpanese, T. Ewalds, R. Hafner, A. Abdolmaleki, D. de Las Casas *et al.*, “Magnetic control of tokamak plasmas through deep reinforcement learning,” *Nature* **602**, 414–419 (2022).
12. V. Sze, Y. Chen, T. Yang, and J. S. Emer, “Efficient processing of deep neural networks: A tutorial and survey,” *Proc. IEEE* **105**, 2295–2329 (2017).
13. V. Sze, Y. Chen, T. Yang, and J. Emer, *Efficient Processing of Deep Neural Networks* (Morgan & Claypool, 2020).
14. A. Sebastian, M. Le Gallo, R. Khaddam-Aljameh, and E. Eleftheriou, “Memory devices and applications for in-memory computing,” *Nat. Nanotechnol.* **15**, 529–544 (2020).
15. C.-X. Xue, Y.-C. Chiu, T.-W. Liu, T.-Y. Huang, J.-S. Liu, T.-W. Chang, H.-Y. Kao, J.-H. Wang, S.-Y. Wei, C.-Y. Lee *et al.*, “A CMOS-integrated compute-in-memory macro based on resistive random-access memory for AI edge devices,” *Nat. Electron.* **4**, 81–90 (2021).
16. V. Joshi, M. Le Gallo, S. Haefeli, I. Boybat, S. R. Nandakumar, C. Piveteau, M. Dazzi, B. Rajendran, A. Sebastian, and E. Eleftheriou, “Accurate deep neural network inference using computational phase-change memory,” *Nat. Commun.* **11** (2020).
17. P. Yao, H. Wu, B. Gao, J. Tang, Q. Zhang, W. Zhang, J. J. Yang, and H. Qian, “Fully hardware-implemented memristor convolutional neural network,” *Nature* **577**, 641–646 (2020).
18. T. P. Xiao, C. H. Bennett, B. Feinberg, S. Agarwal, and M. J. Marinella, “Analog architectures for neural network acceleration based on non-volatile memory,” *Appl. Phys. Rev.* **7**, 031301 (2020).
19. Y. Shen, N. C. Harris, S. Skirlo, M. Prabhu, T. Baehr-Jones, M. Hochberg, X. Sun, S. Zhao, H. Larochelle, D. Englund, and M. Soljačić, “Deep learning with coherent nanophotonic circuits,” *Nat. Photonics* **11**, 441 (2017).
20. A. N. Tait, T. F. de Lima, E. Zhou, A. X. Wu, M. A. Nahmias, B. J. Shastri, and P. R. Prucnal, “Neuromorphic photonic networks using silicon photonic weight banks,” *Sci. Rep.* **7**, 7430 (2017).
21. J. Feldmann, N. Youngblood, M. Karpov, H. Gehring, H. Li, M. Stappers, M. Le Gallo, X. Fu, A. Lukashchuk, A. S. Raja, J. Liu, C. D. Wright, A. Sebastian, T. J. Kippenberg, W. H. P. Pernice, and H. Bhaskaran, “Parallel convolutional processing using an integrated photonic tensor core,” *Nature* **589**, 52–58 (2021).
22. T. P. Xiao, C. H. Bennett, B. Feinberg, S. Agarwal, and M. J. Marinella, “Analog architectures for neural network acceleration based on non-volatile memory,” *Appl. Phys. Rev.* **7**, 031301 (2020).
23. Q. Xia and J. J. Yang, “Memristive crossbar arrays for brain-inspired computing,” *Nat. Mater.* **18**, 309–323 (2019).
24. J. W. Goodman, A. R. Dias, and L. M. Woody, “Fully parallel, high-speed incoherent optical method for performing discrete Fourier transforms,” *Opt. Lett.* **2**, 1–3 (1978).
25. R. A. Athale and W. C. Collins, “Optical matrix–matrix multiplier based on outer product decomposition,” *Appl. Opt.* **21**, 2089–2090 (1982).
26. D. Psaltis and N. Farhat, “Optical information processing based on an associative-memory model of neural nets with thresholding and feedback,” *Opt. Lett.* **10**, 98–100 (1985).
27. K. Wagner and D. Psaltis, “Multilayer optical learning networks,” *Appl. Opt.* **26**, 5061–5076 (1987).
28. J. W. Goodman, “4 decades of optical information processing,” *Opt. Photonics News* **2**, 11–15 (1991).
29. E. N. Leith, “The evolution of information optics,” *IEEE J. Sel. Top. Quantum Electron.* **6**, 1297–1304 (2000).
30. R. Hamerly, L. Bernstein, A. Sludds, M. Soljačić, and D. Englund, “Large-scale optical neural networks based on photoelectric multiplication,” *Phys. Rev. X* **9**, 021032 (2019).
31. L. Bernstein, A. Sludds, R. Hamerly, V. Sze, J. Emer, and D. Englund, “Freely scalable and reconfigurable optical hardware for deep learning,” *Sci. Reports* **11**, 2045–2322 (2021).
32. T. Wang, S.-Y. Ma, L. G. Wright, T. Onodera, B. C. Richard, and P. L. McMahon, “An optical neural network using less than 1 photon per multiplication,” *Nat. Commun.* **13**, 123 (2022).
33. J. Spall, X. Guo, T. D. Barrett, and A. Lvovsky, “Fully reconfigurable coherent optical vector–matrix multiplication,” *Opt. Lett.* **45**, 5752–5755 (2020).
34. T. Zhou, X. Lin, J. Wu, Y. Chen, H. Xie, Y. Li, J. Fan, H. Wu, L. Fang, and Q. Dai, “Large-scale neuromorphic optoelectronic computing with a reconfigurable diffractive processing unit,” *Nat. Photonics* **15**, 367–373 (2021).
35. M. Miscuglio, Z. Hu, S. Li, J. K. George, R. Capanna, H. Dalir, P. M. Bardet, P. Gupta, and V. J. Sorger, “Massively parallel amplitude-only Fourier neural network,” *Optica* **7**, 1812–1819 (2020).
36. X. Lin, Y. Rivenson, N. T. Yardimci, M. Veli, Y. Luo, M. Jarrahi, and A. Ozcan, “All-optical machine learning using diffractive deep neural networks,” *Science* **361**, 1004–1008 (2018).
37. K. Terao, H. Nagai, D. Morita, S. Masui, T. Yanamoto, and S.-i. Nagahama, “Blue and green GaN-based vertical-cavity surface-emitting lasers with AlInN/GaN DBR,” in *Gallium Nitride Materials and Devices XVI*, vol. 11686 (International Society for Optics and Photonics, 2021), p. 116860E.
38. M. Kuramoto, S. Kobayashi, T. Akagi, K. Tazawa, K. Tanaka, T. Saito, and T. Takeuchi, “High-output-power and high-temperature operation of blue GaN-based vertical-cavity surface-emitting laser,” *Appl. Phys. Express* **11**, 112101 (2018).
39. M. Kuramoto, S. Kobayashi, T. Akagi, K. Tazawa, K. Tanaka, K. Nakata, and T. Saito, “Watt-class blue vertical-cavity surface-emitting laser arrays,” *Appl. Phys. Express* **12**, 091004 (2019).
40. W. Dong, H. Liu, J. K. Behera, L. Lu, R. J. H. Ng, K. V. Sreekanth, X. Zhou, J. K. W. Yang, and R. E. Simpson, “Wide bandgap phase change material tuned visible photonics,” *Adv. Funct. Mater.* **29**, 1806181 (2019).
41. M. Delaney, I. Zempakis, D. Lawson, D. W. Hewak, and O. L. Muskens, “A new family of ultralow loss reversible phase-change materials for photonic integrated circuits: Sb₂S₃ and Sb₂Se₃,” *Adv. Funct. Mater.* **30**, 2002447 (2020).

42. K. Gao, K. Du, S. Tian, H. Wang, L. Zhang, Y. Guo, B. Luo, W. Zhang, and T. Mei, "Intermediate phase-change states with improved cycling durability of Sb_2S_3 by femtosecond multi-pulse laser irradiation," *Adv. Funct. Mater.* **31**, 2103327 (2021).
43. A. Rahim, A. Hermans, B. Wohlfeil, D. Petousi, B. Kuyken, D. Van Thourhout, and R. Baets, "Taking silicon photonics modulators to a higher performance level: state-of-the-art and a review of new technologies," *Adv. Photonics* **3**, 024003 (2021).
44. B. Fahs, A. J. Chowdhury, Y. Zhang, J. Ghasemi, C. Hitchcock, P. Zarkesh-Ha, and M. M. Hella, "Design and modeling of blue-enhanced and bandwidth-extended PN photodiode in standard CMOS technology," *IEEE Transactions on Electron Devices* **64**, 2859–2866 (2017).
45. H. Zimmermann, A. Marchlewski, W. Gaberl, I. Jonak-Auer, G. Meinhardt, and E. Wachmann, "Blue-enhanced PIN finger photodiodes in a 0.35- μm SiGe BiCMOS technology," *IEEE Photonics Technol. Lett.* **21**, 1656–1658 (2009).
46. D. A. B. Miller, "Attojoule optoelectronics for low-energy information processing and communications," *J. Light. Technol.* **35**, 346–396 (2017).
47. C. Sun, M. Wade, M. Georgas, S. Lin, L. Alloatti, B. Moss, R. Kumar, A. H. Atabaki, F. Pavanello, J. M. Shainline, J. S. Orcutt, R. J. Ram, M. Popović, and V. Stojanović, "A 45 nm CMOS-SOI monolithic photonics platform with bit-statistics-based resonant microring thermal tuning," *IEEE J. Solid-State Circuits* **51**, 893–907 (2016).
48. B. E. Jonsson, "An empirical approach to finding energy efficient ADC architectures," in *Proc. of 2011 IMEKO IWADC & IEEE ADC Forum*, (2011), pp. 1–6.
49. V. Tripathi and B. Murmann, "An 8-bit 450-MS/s single-bit/cycle SAR ADC in 65-nm CMOS," in *2013 Proceedings of the ESSCIRC (ESSCIRC)*, (IEEE, 2013), pp. 117–120.
50. O. Morales Chacón, J. J. Wikner, C. Svensson, L. Siek, and A. Alvandpour, "Analysis of energy consumption bounds in CMOS current-steering digital-to-analog converters," *Analog. Integr. Circuits Signal Process.* pp. 1–13 (2022).
51. C. Haffner, D. Chelladurai, Y. Fedoryshyn, A. Josten, B. Baeuerle, W. Heni, T. Watanabe, T. Cui, B. Cheng, S. Saha *et al.*, "Low-loss plasmon-assisted electro-optic modulator," *Nature* **556**, 483–486 (2018).
52. M. Burla, C. Hoessbacher, W. Heni, C. Haffner, Y. Fedoryshyn, D. Werner, T. Watanabe, H. Massler, D. L. Elder, L. R. Dalton *et al.*, "500 GHz plasmonic Mach-Zehnder modulator enabling sub-THz microwave photonics," *APL Photonics* **4**, 056106 (2019).
53. P. Kharel, C. Reimer, K. Luke, L. He, and M. Zhang, "Breaking voltage-bandwidth limits in integrated lithium niobate modulators using micro-structured electrodes," *Optica* **8**, 357–363 (2021).
54. Y. Chen, T. Krishna, J. S. Emer, and V. Sze, "Eyeriss: An energy-efficient reconfigurable accelerator for deep convolutional neural networks," *IEEE J. Solid-State Circuits* **52**, 127–138 (2017).
55. Y. S. Shao, J. Clemons, R. Venkatesan, B. Zimmer, M. Fojtik, N. Jiang, B. Keller, A. Klinefelter, N. Pinckney, P. Raina, S. G. Tell, Y. Zhang, W. J. Dally, J. Emer, C. T. Gray, B. Khailany, and S. W. Keckler, "Simba: Scaling deep-learning inference with multi-chip-module-based architecture," in *Proceedings of the 52nd Annual IEEE/ACM International Symposium on Microarchitecture*, (Association for Computing Machinery, New York, NY, USA, 2019), MICRO '52, pp. 14–27.
56. M. Horowitz, "Computing's energy problem (and what we can do about it)," in *2014 IEEE International Solid-State Circuits Conference Digest of Technical Papers (ISSCC)*, (IEEE, 2014), pp. 10–14.
57. A. Stillmaker and B. Baas, "Scaling equations for the accurate prediction of CMOS device performance from 180 nm to 7 nm," *Integration* **58**, 74–81 (2017).
58. F. Kiani, J. Yin, Z. Wang, J. J. Yang, and Q. Xia, "All hardware-based two-layer perceptron implemented in memristor crossbar arrays," in *2021 IEEE International Symposium on Circuits and Systems (ISCAS)*, (IEEE, 2021), pp. 1–5.
59. Y. LeCun, B. Boser, J. S. Denker, D. Henderson, R. E. Howard, W. Hubbard, and L. D. Jackel, "Backpropagation applied to handwritten zip code recognition," *Neural computation* **1**, 541–551 (1989).

Single-Shot Optical Neural Network: Supplemental Document

This document provides supplementary information to the article “Single-Shot Optical Neural Network”. We first describe our latency, energy and throughput calculations. We also give further details on our experimental demonstration: on the optical setup, the implementation of negative weights, the calibration steps and training procedure. Finally, we explain the decrease in classification accuracy with a spectrally broad source and calculate the theoretical accuracy of our system as a function of source bandwidth.

1. LATENCY, ENERGY AND THROUGHPUT OF A NEAR-TERM SYSTEM

The latency of our system is defined by the sum of the latencies of each of the components shown in Fig. S1, where the DAC, modulator, photon time of flight, RC time for electronic summation (parasitics of the TIA), ADC and nonlinearity take ~ 1 ns each (one standard computer clock cycle). Thus, the system operates with a latency on the order of ~ 10 ns for a full matrix-vector computation. As mentioned in the main text, computation is pipelined such that the throughput is defined by the slowest component, yielding 10^6 MACs per ~ 1 ns, i.e., petaMAC/s. The energy consumption for a complete matrix-vector multiplication ($N \times K$ MACs) is the sum of the DAC, TIA, ADC and nonlinearity energies, plus the photon energy required to discriminate 256 levels on the TIA:

$$E_{\text{total}} = N \cdot \frac{1}{\eta_{\text{Laser}} \cdot \eta_{\text{PD}}} \cdot 2^{n_b} \cdot \zeta \cdot t + K \cdot E_{\text{DAC}} + N \cdot (E_{\text{TIA}} + E_{\text{ADC}} + E_{\text{NL}}) \quad (\text{S1})$$

where $\eta_{\text{Laser}} \approx 10\%$ is the source wall-plug efficiency [1–3], $\eta_{\text{PD}} \approx 0.2$ A/W is the PD responsivity [4, 5], $n_b = 8$ bits, $\zeta \approx 1$ μA is the TIA sensitivity at 1 GHz [6], $t = 1$ ns is the integration time and each of the remaining component energies (TIA [6], ADC [7], DAC [8, 9], NL [10, 11]) are 1 pJ per operation. (We assume static weighting with infrequent resets in inference such that weighting energy is negligible.) For $N = K = 1,000$, the energy per MAC ($E_{\text{total}} / (N \cdot K)$) is therefore ~ 10 fJ/MAC. These calculations are summarized in Table S1.

2. EXPERIMENT: DETAILED DESCRIPTION

The first spatial light modulator (SLM, Meadowlark, AVR Optics P1920-400-800-HDMI-T, pixel width 9.2 μm) displays an input image x by modulating the phase of the polarization component of the incident collimated beam that is parallel to the extraordinary axis. (The polarization component along the ordinary axis is unchanged.) Because the light incident on this SLM is polarized at 45° after rotation by the half-wave plates, the SLM effectively performs pixel-wise polarization rotation of the beam. A polarizing beamsplitter (PBS) then rejects the unrotated

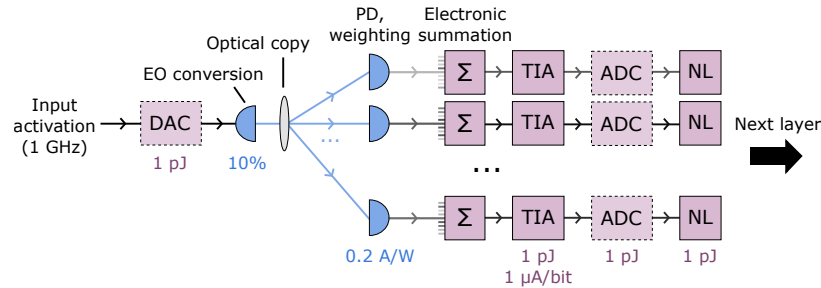


Fig. S1. Path of one input activation through the single-shot ONN in an optimized setup. A VCSEL or μLED converts the signal from the electronic to optical domain and the optical copy is a passive diffractive optical element. Each photodetector (PD) includes a passive weighting element and is electrically connected to K other PDs for analog electronic summation. The nonlinearity is a simple comparator. Each of the K input activations goes through these processing steps simultaneously such that after one pass, the matrix-vector product is complete.

Table S1. Parameters in energy calculation

Symbol	Parameter	Value ¹	Fan-out	Energy/MAC ³
η_{Laser}	Laser wall-plug efficiency	10% [1–3]		
η_{PD}	Photodetector responsivity	0.2 A/W [4, 5]		
n_b	Effective number of bits	8		
ζ	TIA sensitivity	1 μA [6]		
t	Clock cycle time	1 ns		
E_{DAC}	Energy of one DAC conversion	1 pJ [8, 9]	N	1 pJ/ $N \rightarrow$ 1 fJ/MAC
E_{Optical}	Optical energy in one block ²	$\frac{1}{\eta_{\text{Laser}} \cdot \eta_{\text{PD}}} \cdot 2^{n_b} \cdot \zeta \cdot t \approx 10$ pJ	K	10 pJ/ $K \rightarrow$ 10 fJ/MAC
E_{TIA}	Energy of TIA	1 pJ [6]	K	1 pJ/ $K \rightarrow$ 1 fJ/MAC
E_{ADC}	Energy of one ADC conversion	1 pJ [7]	K	1 pJ/ $K \rightarrow$ 1 fJ/MAC
E_{NL}	Energy of nonlinearity	<1 pJ [10, 11]	K	<1 pJ/ $K \rightarrow$ <1 fJ/MAC
E_{total}	Energy of full system	~ 10 nJ	$N \cdot K$	~ 10 nJ/ $(N \cdot K) \rightarrow \sim 10$ fJ/MAC

¹ Demonstrated in the literature² Optical energy for 2^{n_b} distinguishable levels by the TIA³ Assuming $N = K = 1,000$

polarization from the SLM. The input activations are thus encoded into optical intensities through this ‘amplitude-mode’ operation of a ‘phase-only’ SLM. To display the input activations in the first layer of the DNN, we use every second pixel of the SLM and turn every other pixel ‘off’ such that the input pattern is effectively multiplied by a grating. We then block the zero order in the Fourier plane to reduce background noise, such as reflection from the backplane. In subsequent layers with fewer input activations (shorter x), we use every eighth pixel of the SLM to further reduce crosstalk. The incident light on the second SLM (Hamamatsu X10468-04, pixel width 20 μm) is horizontally polarized (along the extraordinary axis); this SLM is in the Fourier plane and adds a variable phase delay to each pixel to impart a fan-out phase pattern. We used the weighted Gerchberg-Saxton algorithm (without camera feedback) to determine the phase pattern [12], which only needed to be calculated once, as it is independent of the weight and input activation values. The third SLM (Meadowlark, AVR Optics P1920-400-800-HDMI-T, pixel width 9.2 μm), in the image plane, is used in ‘amplitude mode’, similarly to the first SLM. Telescopes of achromatic lenses (Thorlabs ACT508-250-A, AC508-180-A, and ACT508-750-A) transmit the replicated input activations to the image planes for 1:1 mapping from SLM #1 to SLM #3 to the camera (Thorlabs DCC3240M, pixel width 5.3 μm). The lens positions along the optical axis are fine-tuned with linear stages. A MATLAB program performs all the control and processing on a digital electronic computer. The supercontinuum source in the throughput experiments is the SuperK EXW-12 from NKT with a VARIA tunable filter.

3. NEGATIVE WEIGHTS

A number of solutions can implement negative weighting. For example, a second wire can connect all the PDs in a block; charge from the negatively weighted pixels would be directed into this second wire with an analog switch. The output from the ‘negative’ wire can then be subtracted from the output of the ‘positive’ wire. Because this subtraction only occurs once per block, its cost is amortized by a factor of K and is therefore small with respect to the other costs of the system. Another possibility for negative weighting is to use two PDs per receiver pixel, where one PD pushes charge into the block’s wire in the case of a positive weight, and another pulls charge in the case of a negative weight. The weight value of the unused photodetector is set to maximum extinction. Lastly, the weights can be shifted to all positive values, as described by Wang et al. [13].

4. CALIBRATION PROCEDURE

The SLM calibrations from the manufacturers are set to map the input values of 0 to 255 linearly to a 0 to 2π phase shift for normally incident 532 nm light. Since we use the SLMs from Meadowlark/AVR Optics (i.e., SLMs #1 and #3) to modulate amplitude and not phase, the output light intensity then varies sinusoidally with input value and requires recalibration. This SLM model has 2048 voltage settings in hardware with $>2\pi$ phase modulation. In the calibration step, we display a uniform array at one voltage value, then average the output intensity map to obtain one output value per input voltage. We then step through the input voltage values linearly through time, and fit the inputs versus averaged outputs with a 9th-order polynomial. We use the resulting lookup table as a global calibration to map desired output intensity to SLM input values. The latter are then restricted to 7-8 bits of precision depending on the intensity region since there are multiple maximum to minimum output intensity cycles within the 2048 available input voltage values. Furthermore, because a wide region of SLM #3 is illuminated, local heating or nonuniformities will cause different blocks (subimages) to require slightly different calibrations to achieve a linear weight display. Therefore, we calculate a refined fit per subimage (8th order polynomial through the origin) after repeating the calibration with the global lookup table generated in the previous step and adjust the displayed weight values accordingly.

We also perform simple processing of the output images from the camera. To reduce the impact of stray light in the system, we acquire a background with SLMs #1 and #3 set to all zeros, and subtract this background from every output frame. We also perform 2×2 pixel binning. Furthermore, the fan-out pattern displayed on SLM #2 does not yield subimages of equal average intensities on the camera. Therefore, we also acquire a calibration map by setting all activations and weights to a constant value. The smoothed and background-subtracted camera output yields the desired map, used for normalization in our experiments. In layer 1, the outputs are also divided by the mean intensity per subimage of 100 randomly selected images from the MNIST validation set. The normalization process reduces the effective number of bits for some subimages since we do not make use of the full dynamic range of the camera. The spot uniformity could be improved by adjusting the pattern on SLM #2 with a feedback algorithm [12], eliminating the need for normalization. In an optimized implementation, the background subtraction can be implemented with a bias voltage.

5. TRAINING

The fully connected neural network was trained on a standard digital computer in Python with the Keras library on a subset of the MNIST training set (50,000 images, where 10,000 images were reserved as a validation set to fine-tune the network hyperparameters as well as the calibration procedure and optical setup). L1 and L2 regularization with $L1 = L2 = 0.0001$, 3% Gaussian noise and 10% dropout were applied to each layer. The nonlinear activation function on the final layer was softmax. The Adam optimizer minimized the categorical crossentropy loss function for 30 epochs.

6. CLASSIFICATION ACCURACY WITH SPECTRALLY BROAD SOURCE

In this section, we discuss the wavelength dependence of our experimental implementation of the single-shot ONN, and then determine the theoretical classification accuracy of our system using a spectrally broad source.

An LCoS SLM imparts a phase shift $\Delta\phi$ of:

$$\Delta\phi(V) = \frac{2\pi}{\lambda}(n_e(V) - n_o)a \quad (S2)$$

where V is voltage, λ is wavelength, n_e is extraordinary refractive index (modulated by V), n_o is ordinary refractive index and a is liquid crystal thickness (but $\Delta\phi$ only applies to the incident field's polarization component that is parallel to the SLM's extraordinary axis) [14].

Because SLMs #1 and #3, in 'amplitude mode', are imaged to the camera, a change in wavelength will simply affect their contrast, and the SLM calibration performed at $\lambda_0 = 532$ nm for output optical intensity versus input value will no longer be perfectly linear. For SLM #2, in phase mode, there is a slight loss of phase contrast for wavelengths different from 532 nm. The main source of error, however, arises because the fan-out spot pattern on the camera $\mathbf{I}(\mathbf{r}_d)$ is the spatial Fourier transform of the SLM #2 pattern $\mathbf{P}(\mathbf{r}_F)$, with an argument of $\mathbf{r}_d = 2\pi \cdot \mathbf{r}_F / (\lambda \cdot f)$. Therefore, the magnification, or distance between spots (in our case, distance between subimages) varies with wavelength.

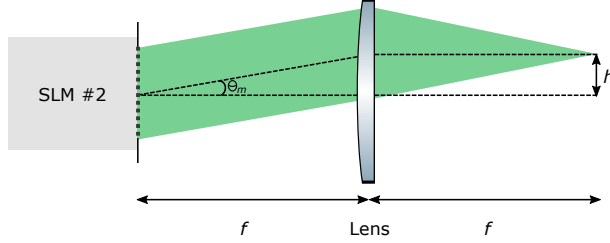


Fig. S2. A collimated beam is diffracted at an angle θ_m by a grating and focused by a lens of focal length f to a distance h from the optical axis.

This concept can be intuitively understood by assuming a simple grating is displayed on SLM #2, illuminated by a collimated beam of wavelength λ , as illustrated in Fig S2. The grating equation shows that the grating will yield an angular offset θ_m for different orders m and grating period d :

$$d \cdot \sin(\theta_m) = m\lambda \quad (\text{S3})$$

Using a lens of focal length f for a spatial Fourier transform from the Fourier plane to the image plane, the height h of the focused spot with respect to the optical axis will be:

$$h = f \cdot \tan(\theta_m) \quad (\text{S4})$$

With $\tan(\theta_m) \approx \sin(\theta_m)$ for small angles:

$$h \approx \frac{f \cdot m\lambda}{d} \quad (\text{S5})$$

The spot height h is therefore approximately linear with λ , which we confirmed experimentally. The grating pattern itself, however, does not change appreciably with wavelength. (Though $\Delta\phi$ varies with λ , the grating period d is constant because it is set by the SLM pixel width; $\Delta\phi$ only affects the phase contrast of the grating, e.g., the ramp height.)

Knowing the original distance $h(\lambda_0)$ in the image plane between a diffracted spot and the zero order, the spot location $h(\lambda)$ at a different wavelength λ is:

$$h(\lambda) \approx (\lambda / \lambda_0) \cdot h(\lambda_0) \quad (\text{S6})$$

Spot locations mark the center of each replicated input image in the image plane — the height and width of each individual replica stays constant since SLM #1 is imaged to the camera and any chromatic aberration would cause blurring from a shift in the position of the focal plane rather than a change in magnification.

We can then estimate the blurring of each replicated input image from an arbitrary source spectrum. We measured the spectra of the SuperK at different VARIA filter bandwidth settings with a custom spectrometer available in our laboratory with a sampling width of 0.7 nm. We corrected these spectra for the wavelength response of our ONN demonstration, which has low transmission outside of wavelengths 460 nm to 560 nm, primarily due to the dielectric mirror of SLM #2. To determine our system's response function, we set the VARIA filter to the narrowest bandwidth. We then swept its center wavelength (every 10 nm from 450 nm to 630 nm) while it was in the source position of our ONN experiment and measured the summed intensity on the camera with SLMs #1 and #3 set to a uniform display. We performed a similar measurement with the spectrometer, where we measured and integrated the SuperK's filtered spectrum at the narrowest bandwidth setting for different center wavelengths. We then estimated our system's wavelength response as the summed ONN camera intensity per wavelength divided by the spectrometer's summed intensity per wavelength. We could then calculate the corrected spectra by multiplying the broad-bandwidth spectra (measured on the spectrometer) by this system response (interpolated). For each sampled wavelength λ in a corrected spectrum (every 0.7 nm), we calculated the expected locations of the subimages $h(\lambda)$ using Eq. S6, where we calculated $h(\lambda_0)$ from the spatial Fourier transform of the pattern displayed on SLM #2 at λ_0 (matched experiment). We then set the intensity of all subimages for this wavelength λ to the intensity of the optical spectrum at λ . We then summed the images of predicted replicated inputs over the entire spectrum to obtain the simulated blurred images, which we fed into our DNN to determine the theoretical inference accuracy (where every layer is blurred following the same procedure).

REFERENCES

1. K. Terao, H. Nagai, D. Morita, S. Masui, T. Yanamoto, and S.-i. Nagahama, "Blue and green gan-based vertical-cavity surface-emitting lasers with alinn/gan dbr," in *Gallium Nitride Materials and Devices XVI*, vol. 11686 (International Society for Optics and Photonics, 2021), p. 116860E.
2. M. Kuramoto, S. Kobayashi, T. Akagi, K. Tazawa, K. Tanaka, T. Saito, and T. Takeuchi, "High-output-power and high-temperature operation of blue gan-based vertical-cavity surface-emitting laser," *Appl. Phys. Express* **11**, 112101 (2018).
3. M. Kuramoto, S. Kobayashi, T. Akagi, K. Tazawa, K. Tanaka, K. Nakata, and T. Saito, "Watt-class blue vertical-cavity surface-emitting laser arrays," *Appl. Phys. Express* **12**, 091004 (2019).
4. B. Fahs, A. J. Chowdhury, Y. Zhang, J. Ghasemi, C. Hitchcock, P. Zarkesh-Ha, and M. M. Hella, "Design and modeling of blue-enhanced and bandwidth-extended pn photodiode in standard cmos technology," *IEEE Transactions on Electron Devices* **64**, 2859–2866 (2017).
5. H. Zimmermann, A. Marchlewski, W. Gaberl, I. Jonak-Auer, G. Meinhardt, and E. Wachmann, "Blue-enhanced pin finger photodiodes in a 0.35- μm SiGe BiCMOS technology," *IEEE Photonics Technol. Lett.* **21**, 1656–1658 (2009).
6. C. Sun, M. Wade, M. Georgas, S. Lin, L. Alloatti, B. Moss, R. Kumar, A. H. Atabaki, F. Pavanello, J. M. Shainline, J. S. Orcutt, R. J. Ram, M. Popović, and V. Stojanović, "A 45 nm CMOS-SOI monolithic photonics platform with bit-statistics-based resonant microring thermal tuning," *IEEE J. Solid-State Circuits* **51**, 893–907 (2016).
7. B. E. Jonsson, "An empirical approach to finding energy efficient ADC architectures," in *Proc. of 2011 IMEKO IWADC & IEEE ADC Forum*, (2011), pp. 1–6.
8. V. Tripathi and B. Murmann, "An 8-bit 450-MS/s single-bit/cycle SAR ADC in 65-nm CMOS," in *2013 Proceedings of the ESSCIRC (ESSCIRC)*, (IEEE, 2013), pp. 117–120.
9. O. Morales Chacón, J. J. Wikner, C. Svensson, L. Siek, and A. Alvandpour, "Analysis of energy consumption bounds in CMOS current-steering digital-to-analog converters," *Analog. Integr. Circuits Signal Process.* pp. 1–13 (2022).
10. V. Sze, Y. Chen, T. Yang, and J. S. Emer, "Efficient processing of deep neural networks: A tutorial and survey," *Proc. IEEE* **105**, 2295–2329 (2017).
11. N. P. Jouppi, C. Young, N. Patil, D. Patterson, G. Agrawal, R. Bajwa, S. Bates, S. Bhatia, N. Boden, A. Borchers *et al.*, "In-datacenter performance analysis of a tensor processing unit," in *Proceedings of the 44th annual international symposium on computer architecture*, (2017), pp. 1–12.
12. D. Kim, A. Keesling, A. Omran, H. Levine, H. Bernien, M. Greiner, M. D. Lukin, and D. R. Englund, "Large-scale uniform optical focus array generation with a phase spatial light modulator," *Opt. Lett.* **44**, 3178–3181 (2019).
13. T. Wang, S.-Y. Ma, L. G. Wright, T. Onodera, B. C. Richard, and P. L. McMahon, "An optical neural network using less than 1 photon per multiplication," *Nat. Commun.* **13**, 123 (2022).
14. C. Rosales-Guzmán and A. Forbes, *How to shape light with spatial light modulators* (SPIE Press, 2017).